Front. Earth Sci. 2022, 16(1): 64–74
https://doi.org/10.1007/s11707-021-0871-3

RESEARCH ARTICLE

Characteristics of extreme rainfall and rainbands evolution of Super Typhoon Lekima (2019) during its landfall

Chunyi XIANG[1,2], Liguang WU (✉)[3], Nannan QIN[3]

1 Key Laboratory of Meteorological Disaster (Ministry of Education), Nanjing University of Information Science and Technology, Nanjing 210044, China
2 National Meteorological Center, Beijing 100081, China
3 Department of Atmospheric and Oceanic Sciences and Institute of Atmospheric Sciences, Fudan University, Shanghai 200433, China

Abstract As one of the most devastating tropical cyclones over the western North Pacific Ocean, Super Typhoon Lekima (2019) has caused a wide range of heavy rainfall in China. Based on the CMA Multi-source merged Precipitation Analysis System (CMPAS)-hourly data set, both the temporal and spatial distribution of extreme rainfall is analyzed. It is found that the heavy rainfall associated with Lekima includes three main episodes with peaks at 3, 14 and 24 h after landfall, respectively. The first two rainfall episodes are related to the symmetric outburst of the inner rainband and the persistence of outer rainband. The third rainfall episode is caused by the influence of cold, dry air from higher latitudes and the peripheral circulation of the warm moist tropical storm. The averaged rainrate of inner rainbands underwent an obvious outburst within 6 h after landfall. The asymmetric component of the inner rainbands experienced a transport from North (West) quadrant to East (South) quadrant after landfall which was related to the storm motion other than the Vertical Wind Shear (VWS). Meanwhile the outer rainband in the vicinity of three times of the Radius of Maximum Wind (RMW) was active over a 12-h period since the decay of the inner rainband. The asymmetric component of the outer rainband experienced two significant cyclonical migrations in the northern semicircle.

Keywords extreme rainfall, rainband evolution, landfalling tropical cyclone

1 Introduction

Tropical cyclones (TCs) accompanied by gale winds, torrential rain, inland flooding or mountainous mudslides are among the most devastating natural disasters in the world (Zhang et al., 2009). In addition to its track and intensity forecasts, one of the most challenging parts, especially for high-impact TCs, is the Quantitative Precipitation Forecast (QPF) for the suffering regions. The ability to forecast heavy rainfall associated with landfalling tropical cyclones (LTCs) can be improved with a better understanding of the heavy rainfall rate and distribution of LTCs (Chen et al., 2010).

Not only LTCs but also TCs in the open oceans exhibit the characteristics of asymmetric rainfall (Corbosiero and Molinnari, 2002; Chan et al., 2004; Lonfat, 2004; Chen et al., 2006; Cecil, 2007). Certain asymmetric rainfall or convective activities can be observed through satellite image or radar rainfall estimation (e.g., Reasor et al., 2013), as well as numerical simulations (e.g., Frank and Ritchie, 2001; Rogers et al., 2003; Wang, 2002a, 2002b). It is believed that in addition to the low-level convergence caused by surface friction associated with storm motion and uneven distribution of ocean thermal condition, environmental VWS around TCs is a fundamental factor to asymmetric rainfall. Recently extensive studies reach a general consensus that the maximum convection as well as heavy rain rate occurs mostly at the downshear left side in the Northern Hemisphere, regardless of the storm motion (e.g., Frank and Ritchie, 2001; Corbosiero and Molinari, 2002; DeHart et al., 2014; Yu et al., 2015; Xu et al., 2014; Yu et al., 2017). Actually, not all observed extreme rainfall distribution can be exactly caused by shear-induced asymmetries, ocean thermal condition (Cecil, 2007; Jiang et al., 2008a and 2008b.), surface friction difference between land and sea (Chen et al., 2006), and also

Received May 19, 2020; accepted January 5, 2021

E-mail: liguangwu@fudan.edu.cn

interactions between TCs and other systems like monsoon (Dong et al., 2010; Chien and Kuo, 2011; Qiu et al., 2020), binary typhoon vortex (Xu et al. 2011), interaction with middle latitude weather systems, or extratropical transition (Meng and Wang, 2016) and local topography (Chien and Kuo, 2011; Liou et al., 2013) could be influencing factors in particular case studies.

Previous studies have investigated the activity of TC rainband and found that the interaction between rainbands and eyewall can affect the intensity and structure of TCs (Barnes et al., 1983; Powell, 1990a and 1990b; Wang, 2002a and 2009; Wang and Wu, 2004). As one of the most significant asymmetric structures in TCs, rainband and its symmetry process may also be one of the reasons for the formation of the outer eyewall (Willoughby et al., 1982; Yang et al., 2007). Numerical simulations further explored the structure and evolution of the spiral rainbands (Powell, 1990a and 1990b; Li and Wang 2012a and 2012b; Moon and Nolan, 2014 and 2015). According to the characteristics and active areas, different rainbands can be divided into inner spiral rainbands and outer spiral rainbands (Wang, 2009). The inner rainbands mainly appear in the inner region of TCs, which is defined as the area within three times of the RMW. Convective activities in long-distance outer rain belts are even more vigorous than those in principal or secondary rainbands (Houze and Robert, 2010).

The distribution of heavy rainfall affected by topography after landfall is mainly due to the differences in the underlying surface between land and sea. At present, the research on the evolution of TC rainfall structure during landfall is still very limited. The local topography will change the distribution of TC precipitation after landfall to a certain extent (Wu et al., 2002; Chen et al., 2004; Yang et al., 2007; Xu et al., 2011). Previous studies have found that changes in the boundary layer friction and the underlying latent heat heating will trigger the interaction between the high vorticity zone generated in front of the storm and the potential vortex region of the eye area. Prior to landfall, maximum precipitation is found to the front and left quadrants of the TC while the front and right quadrants experienced the maximum precipitation after landfall because of the closure of moisture and increased surface roughness (Chan and Liang, 2003). The convection distribution associated with storm movement may partly explain the observed convective asymmetries of post-landfall process. The environmental VWS may be another factor contributing to the large left–right convective asymmetry (Chan et al., 2004).

As one of the most devastating TCs that affecting China in 2019, Super Typhoon Lekima made its first landfall in Zhejiang Province in the early morning of August 10th and triggered a wide range of heavy rainfall from the eastern to north-eastern parts of China. The extreme rainfall distribution prior to, during and post-landfall associated with Lekima presented significant features of asymmetry. In this study, we first identify the temporal and spatial distribution of extreme rainfall of Lekima, and then focus on the symmetric and asymmetric rainfall distribution associated with different rainbands, and finally analyze the possible maintenance mechanism. Due to limited first-hand observation over ocean, most of previous studies on rainfall asymmetry of LTCs normally based on single source of observations, such as TRMM 3B42 (Chen et al., 2006; Molinari and Vollaro, 2010; Reasor et al., 2013; Xu et al., 2014; Yu et al., 2017), which however has less accuracy over land than over the ocean (Yu et al., 2009; Chen and Wu, 2016). This study aims to discuss the distribution of rainbands during landfall process by using a multiple source observation, which avoids underestimation over land and discontinuity along sea-land junction. Section 2 will introduce the multiple source data used in this study. Section 3 will provide an overview of Super Typhoon Lekima, including the temporal and spatial distribution of extreme rainfall. In Section 4, the symmetric and asymmetric distribution of spiral rainbands during Lekima's landfall will be fully analyzed and possible mechanisms to maintain different rainbands will be briefly discussed. Further discussion and main conclusions are drawn in the last two sections.

2 Data and methods

Data used in this study includes the CMA (China Meteorological Administration) Multi-source merged Precipitation Analysis System (CMPAS)-hourly V2.1 data set which combines more than 40000 surface AWS (Automatic Weather Station) in conjunction with Climate Precipitation Centre Morphing (CMORH) precipitation as well as Fengyun Z satellite precipitation estimatio and radar estimation over China. It has a spatial resolution of 0.01 degree (°) and temporal resolution of 1 h (hr) in the Northern Hemisphere. Compared with single-source observations in independent sample test, the CMPAS has smaller deviations, lower root mean square error and higher spatial correlation (Shen et al., 2014). In operation, this data set can better capture certain varying features of hourly precipitation in severe weather events. By combining geostationary satellite, radar observations and rain gauge observations including inland, offshore and on-islands, this multiple-sources fusion data could give a full picture of rainfall structure during their landfall process considering equivalent merging technique over land and sea. Furthermore, the involving of rain gauge observation from local AWS is crucial to depict the detail and fine structure of precipitation especially in coastal and inland areas. We also used intensive AWS gauge observation to testify the extreme rainfall in Section 3.

The environmental parameters are calculated from ERA5 (Fifth generation of ECMWF atmospheric reanalysis of the global climate) data set from ECMWF (data set

available at Climate Copernicus website). As an improvement of the ERA-Interim reanalysis, the ERA5 data set provides hourly estimation of atmospheric, land and oceanic variables with horizontal resolution of 25 km. The VWS is defined as the difference in vector winds calculated between high and low troposphere within a radius of 200–1000 km from TC center. Specifically, the deep VWS is defined as the difference between 200 and 850 hPa, while the high-level (low-level) VWS corresponds to the difference between 200 (500) and 500 (850) hPa. The structure parameter such as the RMW is calculated from ERA5 data set to measure the structure of target typhoon.

In this study, the CMA Best Frack Archive is used to define the location and intensity of Lekima as well as other TCs (Knapp et al., 2010). To describe the subtle structure change during its landfall process, the original data set with positions every 3 h was interpolated into 1 h without any intensity interpolation.

3 Characteristics of extreme rainfall

3.1 An overview of Super Typhoon Lekima

Lekima developed into a tropical storm on 1200 UTC 4 August 2019 to the east of the Philippines. After steadily moving northwest, it experienced a rapid intensification with an increasing of 22 $m \cdot s^{-1}$ over 24 h from1800 UTC 6 to 1800 UTC 7 August. Lekima was finally upgraded to Super Typhoon intensity on 1200 UTC 8 August with a maximum sustained wind speed (MSWS) of 62 $m \cdot s^{-1}$ and a minimum sea level pressure (MSLP) of 915 hPa. Before landfall, it experienced a brief weakening during the daytime of 9 August, which was followed by a steady re-intensification before its first landfall in Zhejiang Province around 1745 UTC 9 August. A special circular double eyewall can be observed (both in radar and satellite images, figure not given) a few hours before landfall. After landfall, the complicated land-surface contrast and increasing friction in the underlying surface triggered a continue decrease of TC intensity. Then Lekima was tracked northward across land, maintaining its tropical storm intensity for more than 3 days. After passed through Zhejiang and Jiangsu Provinces, it entered into Shandong Province and made its second landfall on 1250 UTC 11 August in Qingdao with a MSWS of 23 $m \cdot s^{-1}$ and a MSLP of 980 hPa. After a few hours circling over Bohai Sea and northern part of Shandong peninsula, it made its third landfall around 0300 UTC 12 August over Weifang with a MSWS of 23 $m \cdot s^{-1}$ and a MSLP of 984 hPa. The remnant of Lekima, stuffed by cold air, continued moving northward and finally dissipated after 0600 UTC 13 August.

During Lekima's first landfall, the extremeness of its rainfall is represented by 22 in situ gauge stations which received record-breaking daily precipitation, with 6/15/1 in Zhejiang/Shandong/Jiangsu Province respectively. More than 135 national weather stations exceed its daily precipitation extreme threshold at the same time. Other than extreme daily precipitation, Kuocang Mountain in Zhejiang Province also experienced extreme accumulated precipitation, with an accumulated rainfall of 833 mm. The accumulated precipitation from 0000 UTC 8 to 0000 UTC 13 August over China was given accompanied with its track. It is noticed that the extreme rainfall with accumulated precipitation over 400 mm appeared in two separated areas: one is in the coastal area of Zhejiang Province and the other is in the middle part of Shandong Province. The first extreme rainfall area is around the track of Lekima with the maximum over 800 mm on the mountain terrain and two separated extreme rainfall points to the south of Yellow Mountain which has remarkable lifting effect. However, the second extreme rainfall area in Shandong is confined to the left side of the storm motion. The accumulated rainfall exhibit a structure of spiral feature in the middle part of Shandong.

3.2 Temporal distribution of extreme rainfall

Lekima brought extensive rainfall over the eastern part of China during its first landfall process. The coastal region of Zhejiang Province received severe heavy rainfall caused by its main circulation (Figure not given). To depict the evolution of deep convection as well as extreme rainfall during this landfalling process, this study uses the CMPAS-hourly V2.1 data to capture the temporal and spatial distribution of extreme rainfall. The AWS gauge data are also used to examine the distribution of extreme value.

To figure out the temporal distribution of extreme precipitation, the total coverage of extreme rainfall with different rain rate were given in Fig. 1. The color lines denote 10 $mm \cdot hr^{-1}$, 20 $mm \cdot hr^{-1}$ and 50 $mm \cdot hr^{-1}$, respectively within 800 km radius from the center of Lekima. The first rainfall episode happened in 2100 UTC 9 August, 3 h after landfall, when the coverage of extreme precipitation expanded obviously. The maximum rainrate approached 100 $mm \cdot hr^{-1}$ which may be related with the outburst of deep convection shortly after landfall. And the total coverage of 50 $mm \cdot hr^{-1}$ rainrate was enlarged, so as with that of 20 $mm \cdot hr^{-1}$ and 10 $mm \cdot hr^{-1}$, which could be possibly related to the concentric eyewall structure before landfall. Then the severe rainrate and its coverage underwent a decrease after sunrise. The second growth in the total coverage of extreme rainfall happen around 0800 UTC 10 August, which is about 14 hr after landfall. Furthermore, the availability of moisture could be another important contribution to this outbreak of extreme rainfall, which will be further discussed in the next section. On the second day after landfall, the 10 $mm \cdot hr^{-1}$ and 20 $mm \cdot hr^{-1}$ coverage were much larger than the first peak while 50 $mm \cdot hr^{-1}$ coverage were obviously lower, which

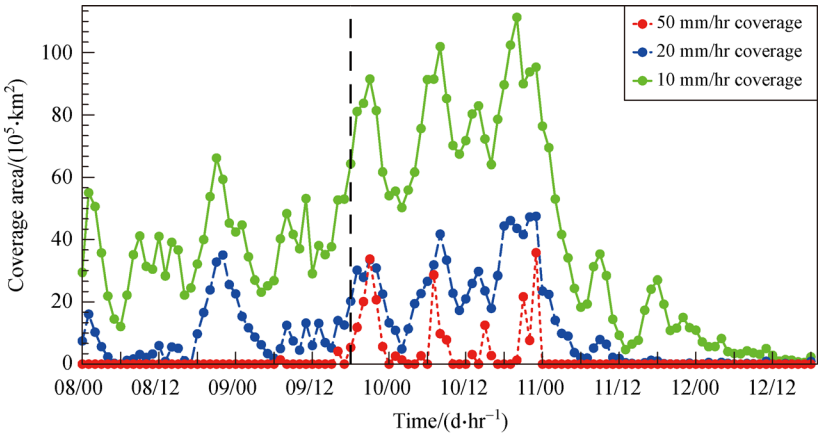

Fig. 1 Time-sequence diagram of coverage area (unit: 10^5 km^2) with different rain rate (green line indicates 10 mm·hr^{-1},blue line indicates 20mm·hr^{-1} and red line indicates 50 mm·hr^{-1})

indicates the extreme rainfall has decreased although the heavy rainfall has expanded compared to the first rainfall episode. The third rainfall episode occurred on the next morning, which is 24 h after landfall, with 10 mm·hr^{-1} rainrate increased significantly, reaching 100000 km^2 while the maximum hourly rainrate are lower than the previous two peaks. The evolution of extreme coverage is characterized by three distinctive rainfall episodes after the first landfall of Lekima in Zhejiang Province.

3.3 Spatial distribution of extreme rainfall

The radial distribution of rainrate was further examined by using intensive rain gauge observation within 800 km radius from the center of Lekima (as shown in Fig. 2). Based on the temporal distribution of rainfall discussed above, the radial rainrate is composited by defined the following three episodes: 1800 UTC 9 Aug to 0200 UTC 10 Aug (as in Fig. 2(a)), 0300 UTC 10 Aug to 1400 UTC 10 Aug (as in Fig. 2(b)) and 1500 UTC 10 Aug to 0600 UTC 11 Aug (as in Fig. 2(c)). In the first rainfall episode, the radial distribution of rainrate represents two distinctive rainband: one is within 50 km from the center accompanied by extreme convective rainfall with maximum rainrate approach 100 mm·hr^{-1}, and the other is around 150 km correspondingly related with the outer spiral rainband which existed since its landfall. There is a magnificent "moat" during this period that can distinguish between inner rainband and outer rainband as the radial structure was not fully collapsed by the surface friction (Frank et al., 1977). In the first rainfall episode, the inner rainband has greater rainrate than that of outer rainband. However, in the second rainfall episode as shown in Fig. 2(b) the inner rainband disappeared with a rapid decrease in rainrate. The outer rainband, on the other side, persisted its distance from the center but obtained an increased rainrate compared to the first rainfall episode. In the second episode, most of the extreme rainfall did not occur in the vicinity of eyewall but happened near the outer rainband. During the third rainfall episode, the former outer rainband did not exist, and most of the extreme rainfall happened more than 200 km from Lekima's center, which corresponds to the distant rainband. Rather than the concentrated convective rainband, the severe rainfall was more dispersed with all of the rainrate declined to less than 80 mm·hr^{-1}. In addition to the radial distribution of extreme rainfall, we will further discuss the evolution of inner and outer rainband in the following section. The radial outflow in the eyewall tilts more outward and transports more hydrometeors generated in the inner region to outer rainband, thereby broadening the surface precipitation area (Yang et al., 2011)

4 Evolution of spiral rainbands

As summarized in the Section 3, the temporal and spatial distribution of extreme rainfall during the landfall process of Lekima could be divided into three episodes. The detail structure evolution of different rainbands related to related three above episodes will be further discussed.

4.1 Symmetric outburst of inner rainband

The azimuthal mean rainrate vary with storm intensity and from basin to basin (Lonfat, 2004). When a TC approaches a terrain like a continent or big island, the asymmetry in low-level winds and precipitation may intensify because of differential forcing between land and ocean. To identify the change of the inner rainbands during landfall, Fig. 3 shows the evolution of axisymmetric mean rainrate and RMW (solid line). As analyzed in Section 3.3, the inner rainband only existed for 6 h after landfall, our analysis covers 24 h prior to and after landfall period from 0600 UTC 9 August to 0600 UTC 10 August. The rainrate within the RMW underwent an obvious outburst within 6 h after landfall

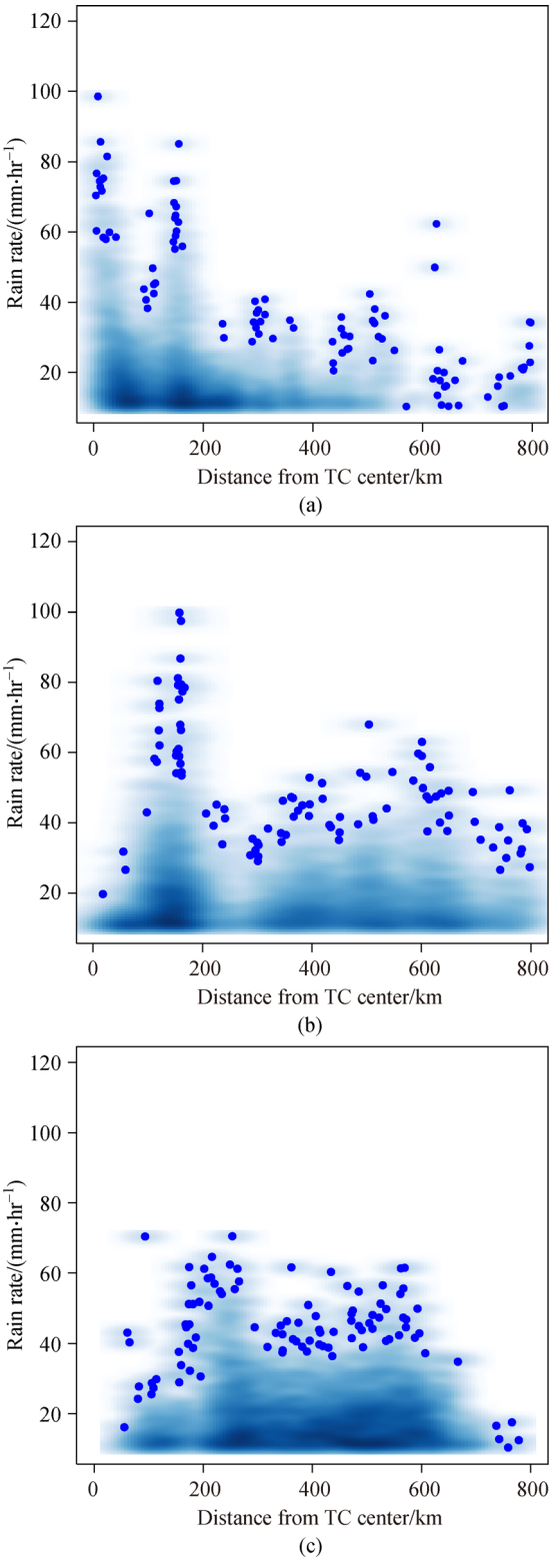

Fig. 2 Radial scatter distribution of rain gauge observed rain rate (units: mm·hr^{-1}) composited from (a) 1800 UTC 9 Aug to 0200 UTC 10 Aug, (b) 0300 UTC 10 Aug to 1400 UTC 10 Aug, (c) 1500 UTC 10 Aug to 0600 UTC 11 Aug. The shaded color represents the probability density of the scatter and blue dots represent singular points.

with maximum rainrate near the TC center. The sudden outburst of rainrate within the RMW is related to the intensified the precipitation efficiency of inner rainbands during landfall. It is also noticed that the RMW represented a steady shrink. Then the RMW followed by a sharp outspread soon after landfall. This shrinking of the RMW is correlated with the re-intensification of Lekima after landfall, which also represents the increasing of inner core deep convection. Other than the outburst rainfall over inner rainband, the outer rainband is captured near 150 km (roughly around the 3 times of RMW) as the defined by Guinn and Schuber (1993) and Wang (2009).

4.2 The asymmetric evolution of rainbands

Figure 4 gives the precipitation distribution during the three extreme rainfall episodes with corresponding storm motion and VWS at previous mentioned three episodes. The most evident feature is that among the three stages, both the inner rainbands and outer rainbands exhibit highly asymmetric structure. During the first outburst of extreme rainfall, most of the heavy rainfall is constrained within 3 times of RMW (Fig. 4(a)). Meanwhile several rain bands are generated along the boundary line between land and sea. Another rainband (L1 in Fig. 4(a)) caused by cold front is located over 800 km at the northwest side from the Lekima. After 11 h, the inner rainbands disappeared and outer rainbands (L3 in Fig. 4(b)) reinforced with asymmetrical maximum rainfall located in the northern semicircle (Fig. 4(b)). It is also observed a long distant rainbands (L2 in Fig. 4(b)). The southeast moving cold front brought its rainbands (L1 in Fig. 4(b)) to encounter that distant rainbands. In the third period of rainfall intensification, both previous inner and outer rainbands are both weakened (Fig. 4(c)). The overlay of cold air and warm moisture delivered by the TC triggered the last outspread of rainfall area (between L1 and L3 in Fig. 4(c)).

In the following work we will further analyze the time evolution of rainband asymmetry. We calculated the asymmetrical components to figure out the evolution of different rainbands. As we already know that the inner rainbands exist within 50 km from the center and the outer rainbands appear around 150 km, the asymmetric and azimuthal mean evolution of inner and outer rainbands are discussed. Figures 5(a) and 5(b) display the time-azimuthal distribution of asymmetric rainfall and symmetric rainrate of inner rainbands respectively. Since the azimuthal mean rainrate receive a remarkable increasing within 6 hr after landfall, the following symmetric mean rainrate decline rapidly after 6 hr. Even though the averaged deep convection collapsed few hours after landfall, the outer rainband maintain active in the north semicircle over 12 hr since the decay of inner rainband. The asymmetric component of inner rainbands experienced a transport from North (West) quadrant to East (South) quadrant in the vicinity of RMW within 12 hr after landfall. This

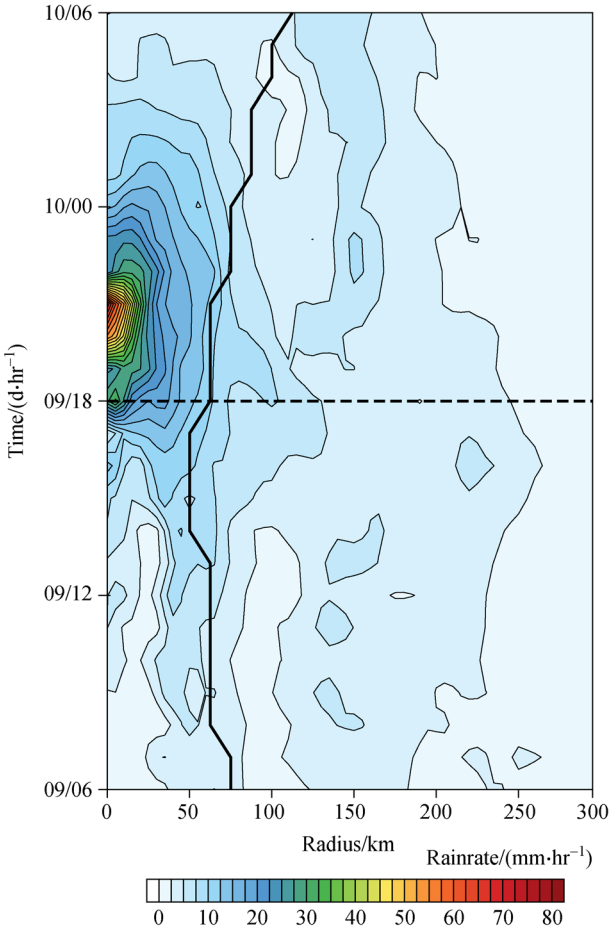

Fig. 3 Time-azimuthal mean distribution of rainrate (unit: mm ·hr^{-1}) within 300 km from storm center; solid line represents the RMW and dash lines represent the landfall.

phenomenon is not appeared before landfall and also not robust in the second day of landfall. The outer rainband has been correspondingly given in Figs. 5(c) and 5(d), which is robust in the vicinity of 150 km but shows no significant asymmetric evolution before landfall. After landfall, it is captured two significant cyclonical transports from East quadrant to North quadrant, than to West quadrant. Each transporting process lasts around 12 hr from East quadrant to West quadrant with declined rainrate along time simultaneously. As discussed in Li's work, the presence of azimuthally asymmetric moist instability is expected to play an important role in fostering and maintaining azimuthally asymmetric convective activity in the outer core of TCs (Li et al., 2020). From the azimuthally asymmetric distribution of θse, the vertical-azimuthal distribution of thermal structure of outer rainband at 0800 UTC 10 Aug is shown in Fig. 6. The northern part of outer rainband bears warmer moisture than its southern part, which will contribute to the maintaining of outer rainband in the northern counterpart. The tangential wind at low level accelerate in the northern quarter other than the

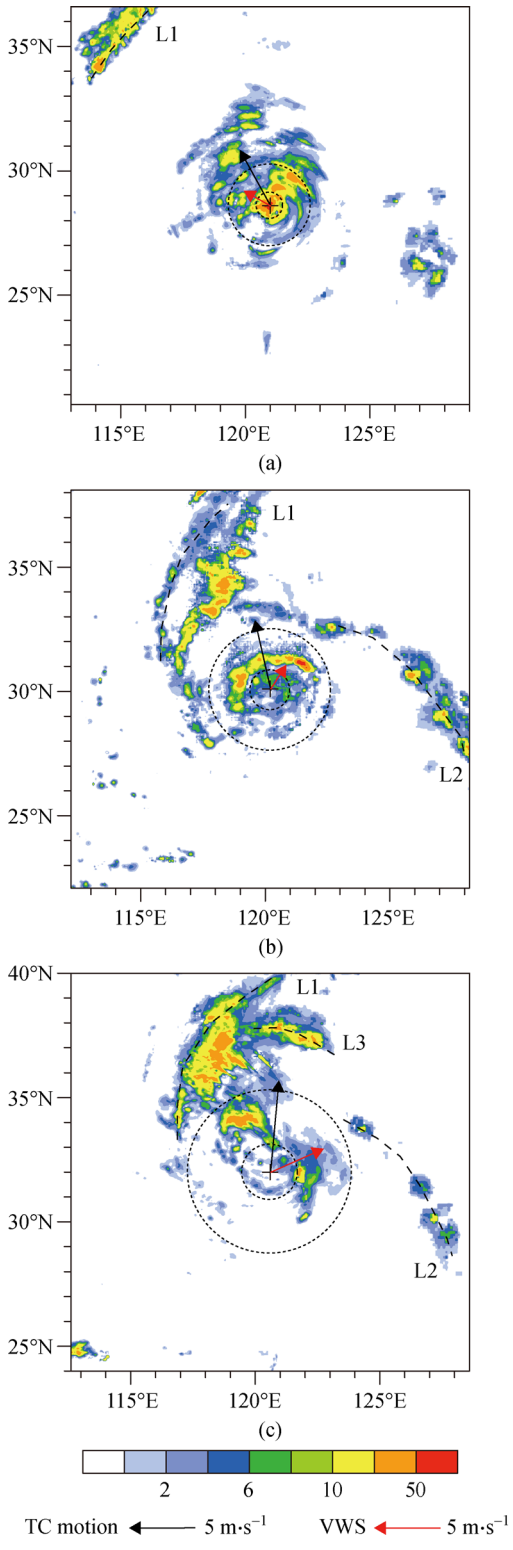

Fig. 4 Rainrate (mm·hr^{-1}) distribution within 800 km radius from the center at 21:00 UTC 9 Aug (a), 08:00 UTC 10 Aug (b), 21:00 UTC 10 Aug (c); read typhoon symbol represents the location of storm center; red and black arrows represent TC motion and vertical wind shear (200–850 hPa), the inner/outter dotted circle indicating the RMW/3RMW and L1, L2, L3 representing the spiral rainband.

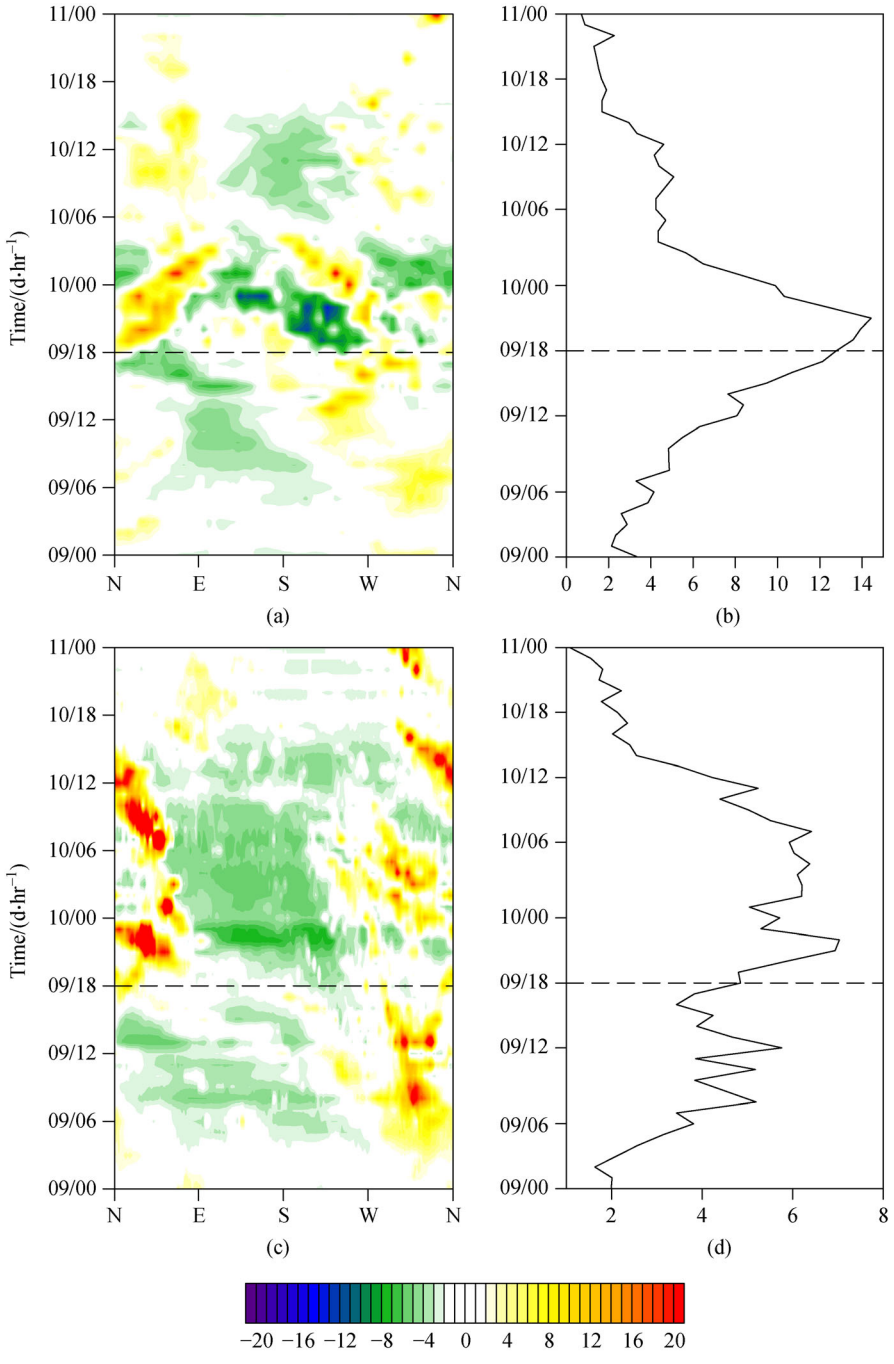

Fig. 5 Time-azimuthal distribution of asymmetric rainrate (a and c) and symmetric rainrate (b and d) (unit: mm·hr^{-1}) of inner rainband (a and b) and outer rainband (c and d) with dash lines indicating the landfall time.

southern part, thus release more energy at the northern counterpart simultaneously.

As VWS is generally considered to be a significant environmental factor in TC structure and intensity change which favored deep convection as well as higher precipitation in the downshear-left quadrant. We further examine the environmental impact during the landfall process of Lekima by using the ERA5 reanalysis. As shown in Fig. 7, the deep VWS (200–850 hPa) as well as the upper level (200–500 hPa) and low level (500–850 hPa) shear all show a remarkable decrease before landfall at 1800 UTC 9 August, then followed by a steady increasing. The direction of VWS also appears a sudden turning from northwest (prior to landfall) to southeast (within few hours after landfall) then back to southwest (12 hr after landfall). Although the hourly ERA5 data might not include in subtle vibration in the direction of VWS, the environmental VWS in deed experienced an

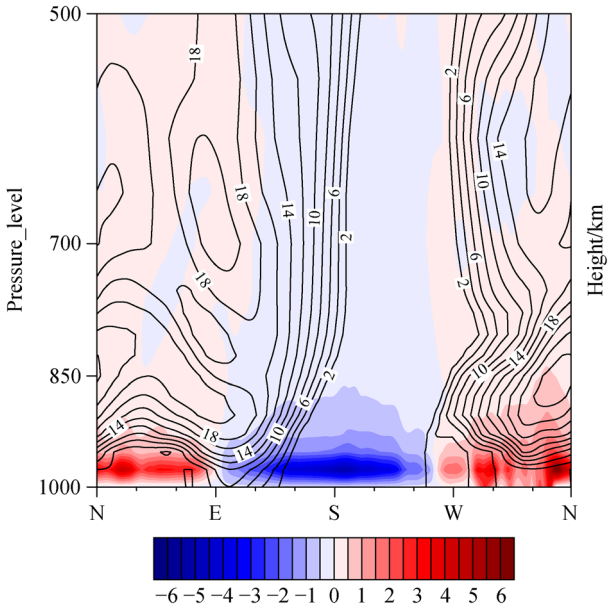

Fig. 6 The vertical-azimuthal distribution of θse deviation (shaded, unit: °C) and tangential wind (contour, m/s) along the outer rainband.

overturn during the landfall process.

During the first rainfall episode, the environmental VWS is less than 6 $m \cdot s^{-1}$ which favors the symmetric of eyewall. However the direction of VWS during this stage is not consisting in one side. The favorable environmental VWS is beneficial to the outburst of inner rainband; however the asymmetric evolution of inner rainband is more related to the TC motion in this respective case. In the second episode of extreme rainfall, in which the outer rainband is active in the northern semicircle. The environmental VWS persist in southwest direction, the asymmetric of outer rainbands is transport from the downshear-right to downshear-left. As discussed in previous work, the presence of azimuthally asymmetric moist instability is expected to play an important role in fostering and maintaining azimuthally asymmetric convective activity in the outer core of TCs (Li and Dai, 2020). The northern semicircle of outer rainbands sinks in warmer moisture than its southern part, which will contribute to the maintenance of outer rainbands in the northern counterpart. Actually during the landfalling of Lekima, the dominant water vapor transport at 850 hPa is from East China Sea. The existing of abundant water vapor, resulting from sustained eastern or southeasterly winds at low level, is a favorable condition for the outburst of inner rainband and maintenance of outer rainbands. The mountain terrain in the coastal region of Zhejiang Province is also anther favorable condition for the reinforcement of heavy rainfall.

5 Discussion

As discussed in previous work, the axisymmetric rainrate during landfalling TCs is related to both TC intensity and

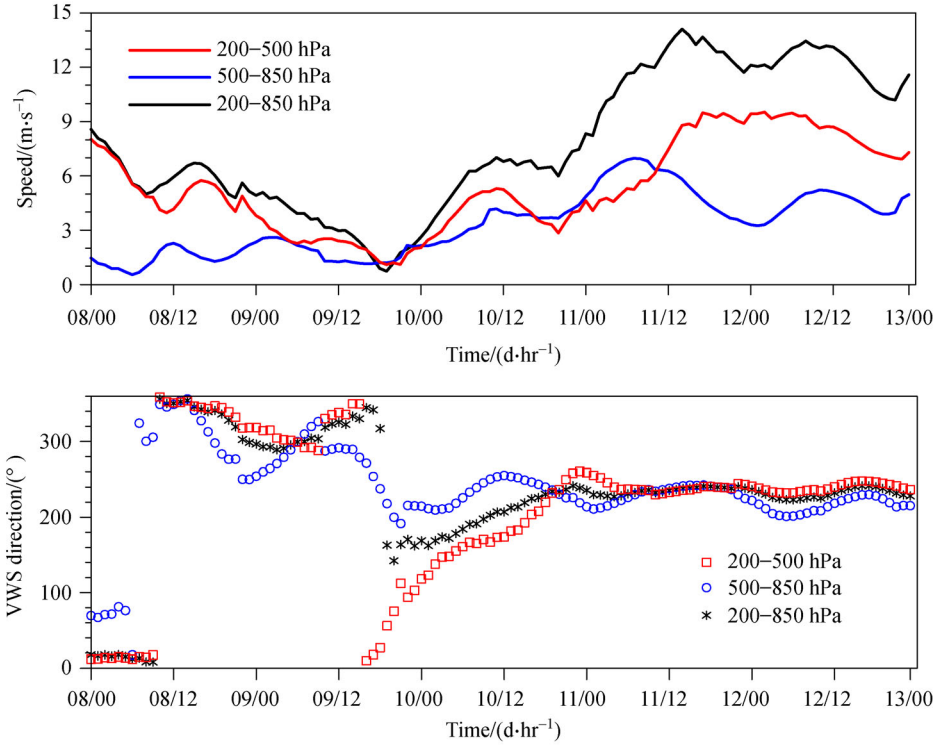

Fig. 7 The magnitude (top, $m \cdot s^{-1}$) and direction (bottom, °) of the vertical wind shear.

intensity change (Yu et al., 2017). We also chose 24 LTCs in China including landfall in Taiwan or Chinese mainland from 2015 to 2018. Because the primary impact of terrorism to LTCs rainfall structure change were mostly related to their first landfall after all. For those LTCs who had a second even a third landfall, only their first landfalls were included. To maintain sufficient analyzed period, TCs which can sustain at least 12 h after landfall were included. To discuss the relation between landfall intensity and symmetric rainrate of inner rainbands, the 24 LTCs were categorized into TD/TS, CAT12 and CAT345 by their landfall intensity. It is further analyzed the azimuthal mean rainrate within 3RMW during their first landfall process (Fig. 8). The results show that most of LTCs experience a remarkable increase of asymmetric rainrate over inner rainbands. On average, the rainrate of inner rainbands all underwent an obvious outburst within 6 h after landfall with maximum rainrate existing near the TC center. The amplitude of such increasing is related to the landfall intensity. LTCs of higher landfall intensity have higher peak azimuthal-mean rainrate than the lower ones. Among those LTCs, Lekima has the strongest landfall intensity, which is followed by a most remarkable increase in the asymmetric rainfall after landfall.

It is also noticed that only the first two stages have been fully discussed due to the motivation of this work, although the extreme rainfall after landfall of Lekima has been divided into three episodes. We mainly focused in the rainbands evolution during the landfall process of Lekima; however the third rainfall episode comprehensively results from the encounter of cold dry air from mid-high latitude system and the peripheral circulation of warm moist tropical storm. More research should be continued in the refine structure of different rainband during the landfall process to uncover the possible maintain and evolution process of LTC rainband.

6 Conclusions

Super Typhoon Lekima (2019) is one of the most devastating TCs over the western North Pacific in recent years. The in situ gauge observations in Zhejiang and Shandong provinces have received extreme rainfall due to the landfall of Lekima and corresponding interaction with mid-latitude system. To study the characteristics of extreme rainfall and its rainbands evolution of LTC, a multiple source of high resolution precipitation data set was used in this paper to discuss the detail extreme rainfall distribution prior to, during and post-landfall associated with Lekima.

First of all, the temporal and spatial distribution of extreme rainfall associated with Lekima was given. It is concluded that there are three main rainfall episodes since its first landfall, with coverage and rainrate peaks at 3, 14 and 24 h after landfall respectively. The evolutions of

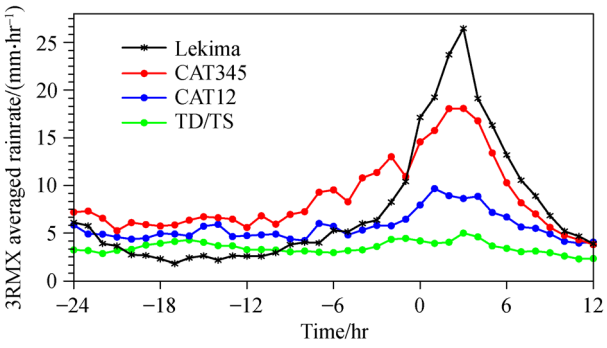

Fig. 8 Time series of the rain rate averaged within the three times of the radius of maximum wind (unit: mm·hr^{-1}) relative to the landfall time for TD/TS (green), CAT12 (blue), CAT345 (red) and Super Typhoon Lekima (black).

extreme coverage are characteristic by three distinctive rainfall episodes after the first landfall of Lekima in Zhejiang Province. Further discussions focus on the evolution of inner rainbands after landfall. It is shown that the averaged rainrate of inner rainbands underwent an obvious outburst within 6 h after landfall with maximum rainrate existed near the TC center. The sudden outburst of rainrate not only appeared in the case of Lekima but also exist in multiple samples composite of LTCs in recent years. This means that rainrate outburst is related to the intensified precipitation efficiency of inner rainbands during landfall along with the steady shrink of RMW respectively. The similar phenomenon has been provided in previous work (Wu et al., 2010), in which six typhoons making landfall along the southeastern coast of China have been selected to examine changes in the precipitation distribution of the azimuthally mean reflectivity. Their results also found that when typhoon are approaching the coast, the mean rainfall rate in the inner-core region increases abruptly and accompanied by the rapid contraction of the out-ring precipitation toward typhoon center. The asymmetric component of inner rainbands experienced a transport from North (West) quadrant to East (South) quadrant in the vicinity of RMW within 12 hr after landfall. It is found that the deep VWS experienced a remarkable decrease before landfall at 1800UTC 9th, which is a favorable condition for the shrink of RMW and convective bursts in the vicinity of eyewall during the first few hours after landfall process. However the direction of VWS during this stage is not consistent in one side. The favorable environmental VWS is beneficial to the outburst of inner rainband, but the asymmetric evolution of inner rainband is more related to the TC motion in the case of Lekima.

During the second episode of extreme rainfall, in which the outer rainband is active in the northern semicircle, the outer rainbands is robust in the vicinity of 3RMW from storm center and captured two significant cyclonical migrations from East to West quadrant while the environ-

mental VWS persist in southwest direction. The asymmetric of outer rainbands is shifted from the downshear-right to downshear-left. Each transition from East quadrant to West quadrant lasts around 12 hr with decreasing rainrate simultaneously. This significant structure change of outer rainbands could be related to the cyclonical development and transition of deep convection cells along this existing rainband.

Finally, the third episode that occurred 24 hr after landfall is due to the encounter of cold dry air from mid-high latitude and the impact of warm and moist peripheral circulation of storm. During this period, the coverage of remote rainbands expanded, but the rainfall rate was lower than the previous two.

Acknowledgements This work was supported by Postdoctoral Science Foundation of China (No. 2019M661342).

References

Barnes G M, Zipser E J, Jorgensen D, Marks F Jr (1983). Mesoscale and convective structure of a hurricane rainbands. J Atmos Sci, 40(9): 2125–2137

Cecil D J (2007). Satellite-derived rain rates in vertically sheared tropical cyclones. Geophys Res Lett, 34(2): L02811

Corbosiero K L, Molinari J (2002). The effects of vertical wind shear on the distribution of convection in tropical cyclones. Mon Weather Rev, 8(130): 2110–2123

Chan J C L, Liang X D (2003). Convective asymmetries associated with tropical cyclone landfall. Part I: f-Plane simulations. Journal of the Atmospheric. Science, 60: 1560–1576

Chan J C L, Liu K S, Ching S E, Lai E S T (2004). Asymmetric distribution of convection associated with tropical cyclones making landfall along the south China coast. Monthly Weather Review, 132 (10): 2410–2420

Chen Y, & Yau M K (2003). Asymmetric structures in a simulated landfalling hurricane. J Atmos Sci, 60(18): 2294–2312

Chen L, Z Luo, Y Li (2004). Research advances on tropical cyclone landfall process. Acta Meteor Sin 62: 541–549.

Chen S S, Knaff J A, Marks F D (2006). Effects of vertical wind shear and storm motion on tropical cyclone rainfall asymmetric deduced from TRMM. Mon Weather Rev, 134(3): 3190–3208

Chen L, Li Y, Cheng Z (2010). An overview of research and forecasting on rainfall associated with landfalling tropical cyclones. Adv Atmos Sci, 27(5): 967–976

Chen X , L Wu (2016). Topographic influence on the motion of tropical cyclones landfalling on the coast of China. Weather and Forecast, 31 (5): 1615–1623

Chien F C, Kuo H C (2011). On the extreme rainfall of typhoon morakot (2009). J Geophys Res, 116(D5): D05104

DeHart J C, Houze R A Jr, Rogers R F (2014). Quadrant distribution of tropical cyclone inner-core kinematics in relation to environmental shear. J Atmos Sci, 71(7): 2713–2732

Dong M, Chen L, Li Y, Lu C (2010). Rainfall reinforcement associated with landfalling tropical cyclones. J Atmos Sci, 67(11): 3541–3558

Frank W M (1977). The structure and energetics of the tropical cyclone I: storm structure. Mon Weather Rev, 105:1119–1135

Frank W M, Ritchie E A (2001). Effects of vertical wind shear on the intensity and structure of numerically simulated hurricanes. Mon Weather Rev, 129(9): 2249–2269

Guinn T A, Schuber W H (1993): Hurricane spiral bands. Journal of the Atmospheric Sciences, 50: 3380–3403

Houze A, Robert (2010). Clouds in tropical cyclones. Monthly Weather Review, 138(2), 293–344

Jiang H, Halverson J B, Simpson J (2008a). On the differences in storm rainfall from hurricanes Isidore and Lili. part I: satellite observations and rain potential. Weather Forecast, 23(1): 29–43

Jiang H, Halverson J B, Zipser E J (2008b). Influence of environmental moisture on TRMM-derived tropical cyclone precipitation over land and ocean. Geophys Res Lett, 35(17): L17806

Knapp K R, Kruk M C, Levinson D H, Diamond H J, Neumann C J (2010). The international best track archive for climate stewardship (IBTrACS). Bull Am Meteorol Soc, 91(3): 363–376

Lee C S, Chen B F, Elsberry R L (2012). Long-lasting convective system in the outer region of tropical cyclones in the western North Pacific. Geophys Res Lett, 39(21): 21812

Lonfat M (2004). Precipitation distribution in tropical cyclones using the tropical rainfall measuring mission (TRMM) microwave imager: a global perspective. Health Res Policy Syst, 11(1): 40–40

Liou Y C, Wang T C C, Tsai Y C, Tang Y S, Lin P L, Lee Y A (2013). Structure of precipitating systems over Taiwan's complex terrain during Typhoon Morakot (2009) as revealed by weather radar and rain gauge observations. J Hydrol (Amst), 506: 14–25

Li Q, Wang Y (2012a). Formation and quasi-periodic behavior of outer spiral rainbands in a numerically simulated tropical cyclone. J Atmos Sci, 69(3): 1333

Li Q, Wang Y (2012b). A comparison of inner and outer spiral rainbands in a numerically simulated tropical cyclone. Mon Weather Rev, 140 (9): 2782–2805

Li Q, Dai Y (2020). Revisiting azimuthally asymmetric moist instability in the outer core of sheared tropical cyclones. Mon Weather Rev, 148: 1297–1319

Meng W, Wang Y (2016). A diagnostic study on heavy rainfall induced by Typhoon Utor (2013) in south China. part I: rainfall asymmetry at landfall. Journal of Geophysical Research Atmospheres

Molinari J, Vollaro D (2010). Distribution of helicity, CAPE and shear in tropical cyclones. J Atmos Sci, 67: 274–284

Moon Y, Nolan D S (2014). Spiral rainbands in a numerical simulation of Hurricane Bill (2009). Part I: structures and comparisons to observations. Journal of the Atmospheric Ences, 72(1): 140908105846009

Moon Y, Nolan D S (2015). Spiral rainbands in a numerical simulation of hurricane bill (2009). Part II: propagation of inner rainbands. J Atmos Sci, 72(1): 191–215

Powell M D (1990a). Boundary layer structure and dynamics in outer hurricane rainbands. Part I: mesoscale rainfall and kinematic structure. Mon Weather Rev, 118(4): 891–917

Powell M D (1990b). Boundary layer structure and dynamics in outer hurricane rainbands. Part II: downdraft modification and mixed layer recovery. Mon Weather Rev, 118(4): 918–938

Qiu W, Wu L, Ren F (2020). Monsoonal influences on offshore rapid

intensification of landfalling typhoon in a sheared environment over South China Sea. Weather Forecast, 35(2): 623–634

Reasor P D, Rogers R, Lorsolo S (2013). Environmental flow impacts on tropical cyclone structure diagnosed from airborne Doppler radar composites. Mon Weather Rev, 141(9): 2949–2969

Rogers R, Chen S, Tenerelli J, Willoughby H (2003). A numerical study of the impact of vertical shear on the distribution of rainfall in Hurricane Bonnie (1998). Mon Weather Rev, 131(8): 1577–1599

Shen Y, Zhao P, Pan Y, Yu J (2014). A high spatiotemporal gauge-satellite merged precipitation analysis over china. J Geophys Res D Atmospheres, 119(6): 3063–3075

Wang Y (2002a). Vortex Rossby waves in a numerically simulated tropical cyclone. Part I: Overall structure, potential vorticity, and kinetic energy budgets. J Atmos Sci, 59(7): 1213–1238

Wang Y (2002b). Vortex Rossby waves in a numerically simulated tropical cyclone. Part II: The role in tropical cyclone structure and intensity changes. J Atmos Sci, 59(7): 1239–1262

Wang Y, Wu C C (2004). Current understanding of tropical cyclone structure and intensity changes – a review. Meteorol Atmos Phys, 87 (4): 257–278

Wang Y (2009). How do outer spiral rainbands affect tropical cyclone structure and intensity? J Atmos Sci, 66(5): 1250–1273

Willoughby H E, Clos J A, Shoreibah M G (1982). Concentric eye walls, secondary wind maxima and the evolution of the hurricane vortex. J Atmos Sci, 39(2): 395–411

Wu C C, Yen T H, Kuo Y H, Wang W (2002) Rainfall simulation associated with Typhoon Herb (1996) near Taiwan. Part I: the topographic effect. Wea Forecasting, 17: 1001–1015

Wu D, Zhao K, Yu H, Wang M J (2010). An analysis of spatial and temporal variations in the axisymmetric precipitation structure associated with typhoon making landfall on the southeastern coast of China based on the Doppler radar data. Acta Meteorol Sinica, 68 (6): 896–907

Xu X, Lu C, Xu H, Chen L (2011). A possible mechanism responsible for exceptional rainfall over Taiwan from Typhoon Morakot. Atmospheric Ence Let, 12

Xu W, Jiang H, Kang X (2014). Rainfall asymmetries of tropical cyclones prior to, during, and after making landfall in south China and southeast United States. Atmos Res, 139(3): 18–26

Yang B, Wang Y, Wang B (2007). The effect of internally generated inner-core asymmetries on tropical cyclone potential intensity. J Atmos Sci, 64(4): 1165–1188

Yang M J, Zhang D L, Tang X D, Zhang Y (2012). A modeling study of Typhoon Nari (2001) at landfall: 2. structural changes and terrain-induced asymmetries. J Geophy Res Atmospheres, 116(D9)

Yu Z, Chen P, Qian C, Yue C (2009). Verification of tropical cyclone-related satellite precipitation estimates in Chinese mainland. J Appl Met Clim, 48: 2227–2241

Yu Y, Wang Y, Xu H, Davidson N, Chen Y, Chen Y, Yu H (2017). On the relationship between intensity and rainfall distribution in tropical cyclones making landfall over China. J Appl Meteorol Climatol, JAMC-D-16–0334.1

Yu Z, Wang Y, Xu H (2015). Observed rainfall asymmetry in tropical cyclones making landfall over China. J Appl Meteorol Climatol, 54 (1): 117–136

Zhang Q, Wu L, Liu Q (2009). Tropical cyclone damages in china 1983–2006. Bull Am Meteorol Soc, 90(4): 489–496